NANOMATERIALS

Critical differences in 3D atomic structure of individual ligand-protected nanocrystals in solution

Byung Hyo Kim[1,2]*, Junyoung Heo[1,2]*, Sungin Kim[1,2], Cyril F. Reboul[3,4], Hoje Chun[5], Dohun Kang[1,2], Hyeonhu Bae[6], Hyejeong Hyun[7], Jongwoo Lim[7], Hoonkyung Lee[6], Byungchan Han[5], Taeghwan Hyeon[1,2], A. Paul Alivisatos[8,9,10], Peter Ercius[11]†, Hans Elmlund[3,4]†, Jungwon Park[1,2]†

Precise three-dimensional (3D) atomic structure determination of individual nanocrystals is a prerequisite for understanding and predicting their physical properties. Nanocrystals from the same synthesis batch display what are often presumed to be small but possibly important differences in size, lattice distortions, and defects, which can only be understood by structural characterization with high spatial 3D resolution. We solved the structures of individual colloidal platinum nanocrystals by developing atomic-resolution 3D liquid-cell electron microscopy to reveal critical intrinsic heterogeneity of ligand-protected platinum nanocrystals in solution, including structural degeneracies, lattice parameter deviations, internal defects, and strain. These differences in structure lead to substantial contributions to free energies, consequential enough that they must be considered in any discussion of fundamental nanocrystal properties or applications.

The three-dimensional (3D) atomic arrangement of materials determines their physical and catalytic properties (*1*, *2*). The 3D structures of nanocrystals typically deviate from the periodic atomic arrangement of their bulk counterparts owing to the dominance of surface dangling bonds, defects, and dislocations, as well as intrinsic quantum effects due to finite size (*3*–*5*). Such deviations are more pronounced in small nanocrystals that have diameters less than 4 nm. For example, interatomic distances near the surface of Au nanocrystals are shortened compared with the perfect face-centered cubic (fcc) structure of bulk Au (*6*), whereas cerium oxide nanocrystals show extended interatomic distances near the surface (*7*). Au nanoparticles below a critical size can have an icosahedral structure that is thermodynamically unfavored in the bulk counterpart (*8*). These distinctive physical properties make nanocrystals attractive as heterogeneous catalysts (*9*). Populations of synthesized nanocrystals tend to have heterogeneous atomic structures because uniform control at the level of individual nanocrystals is extremely difficult to accomplish (*10*, *11*). The organic ligands and solvents used in a typical colloidal synthesis coordinate surface atoms and further affect the crystal and electronic structures of nanocrystals (*12*–*16*). Thus, understanding their distinctive properties requires precise and reproducible determination of the positions of the individual atoms at the level of a single nanocrystal directly from the solution phase, in which most of the catalytic and chemical reactions occur.

The 3D atomic structures of nanocrystals can be determined by electron tomography, whereby the structures are reconstructed from a tilt series of transmission electron microscopy (TEM) images (*17*–*20*). However, this method relies on image acquisition under vacuum and on a substrate, which can cause structural deformation of the nanocrystals. Furthermore, the spatial resolution is frequently nonuniform in 3D space owing to missing projection directions (*21*). Single-particle reconstruction based on cryo-TEM, as an alternative approach, is also not appropriate for studying heterogeneous nanocrystal populations because the analysis relies on 2D images collected from a large number of different particles assumed to have the same structure (*22*). We previously introduced 3D SINGLE (structure identification of nanoparticles by graphene liquid cell electron microscopy) as a direct method to resolve 3D structures of nanocrystals in solution, but the resolution obtained was only sufficient to determine overall morphologies in 3D (*23*) and the understanding of how to analyze such information to extract key structure factors was still limited.

We developed a "Brownian one-particle reconstruction" method—atomic-resolution 3D SINGLE—and applied it to analyze the 3D atomic arrangements of individual Pt nanocrystals in solution. Our high-resolution 3D density maps of eight individual Pt nanocrystals from the same synthesis batch and fitted atomic models show fcc structures with structural heterogeneity, including single-crystallinity, distortion, and dislocation. The precise assignment (±19 pm) of the 3D atomic positions allowed direct investigation of lattice expansion, internal defects, strain near the surfaces and dislocation planes, and their contribution to the free energy. The resulting information shows that structural information obtained in a realistic solution based on the SINGLE method can provide a vital new guide for future improved synthesis and for understanding the properties of the current materials.

3D reconstruction from electron microscopy images of Pt nanocrystals in liquid

Atomic-resolution 3D SINGLE of nanocrystals in solution was achieved through aberration-corrected TEM imaging, by using a direct electron detector with high temporal (2.5 ms) resolution (fig. S1). The high temporal resolution allowed us to capture projection images of the nanocrystals in different views as they were tumbling in solution. The individual particles were tracked throughout the time series, and the extracted trajectories of 2D images were reconstructed to obtain Coulomb charge 3D density maps of the individual particles (see supplementary materials and movie S1). Obtaining thousands of high-resolution images within a few seconds allowed complete coverage of the projection angles, which is required for accurate 3D reconstruction. The 3D orientations of the projections of the randomly rotating nanocrystals were determined using an iterative Fourier 3D reconstruction algorithm based on stochastic hill climbing (*24*). To overcome uncertainties originating from the random movement and innate noise in the TEM images, we developed algorithms for motion correction and subtraction of the background introduced by the liquid cell (see supplementary materials). These are key steps in the advanced 3D reconstruction algorithm to obtain high-resolution 3D density maps.

Representative Pt nanocrystal density maps are depicted in Fig. 1A and movie S2. The reconstructed 3D density maps of the nanocrystals have resolutions better than 0.72 Å, according to the 0.143 Fourier shell correlation criterion (fig. S2) (*25*), allowing assignment of the positions of all constituent atoms in 3D space within the domain of each nanocrystal (Fig. 1B and figs. S3 to S5). The assigned atomic coordinates can further be used to calculate the formation energy of individual nanocrystals (table S1). We obtained strain maps from the atomic position information, which indicate the lattice distortion (Fig. 1C and fig. S6). Sliced 3D maps provide detailed structural information and strain tensors (an

[1]Center for Nanoparticle Research, Institute for Basic Science (IBS), Seoul 08826, Republic of Korea. [2]School of Chemical and Biological Engineering and Institute of Chemical Processes, Seoul National University, Seoul 08826, Republic of Korea. [3]Department of Biochemistry and Molecular Biology, Biomedicine Discovery Institute, Monash University, Clayton, VIC 3800, Australia. [4]ARC Centre of Excellence for Advanced Molecular Imaging, Clayton, VIC 3800, Australia. [5]Department of Chemical and Biomolecular Engineering, Yonsei University, Seoul 03722, Republic of Korea. [6]Department of Physics, Konkuk University, Seoul 05029, Republic of Korea. [7]Department of Chemistry, Seoul National University, Seoul 08826, Republic of Korea. [8]Department of Chemistry, University of California, Berkeley, CA 94720, USA. [9]Material Sciences Division, Lawrence Berkeley National Laboratory, Berkeley, CA 94720, USA. [10]Kavli Energy NanoScience Institute, Berkeley, CA 94720, USA. [11]National Center for Electron Microscopy, Molecular Foundry, Lawrence Berkeley National Laboratory, Berkeley, CA 94720, USA.
*These authors contributed equally to this work.
†Corresponding author. Email: percius@lbl.gov (P.E.); hans.elmlund@monosh.edu (H.E.); jungwonpark@snu.ac.kr (J.P.)

example for one Pt nanocrystal is shown in Fig. 1D).

The reconstruction method and resulting 3D maps were validated in several ways (see supplementary materials). First, the algorithm was verified by reconstructing multislice simulated TEM images of model fcc nanocrystals with 2.5- and 4.0-nm diameters with varying parameters, including different pixel resolutions and binning processes, to mimic the imaging mechanism in TEM (figs. S7 to S9) (*26*). To confirm the robustness of the reconstruction

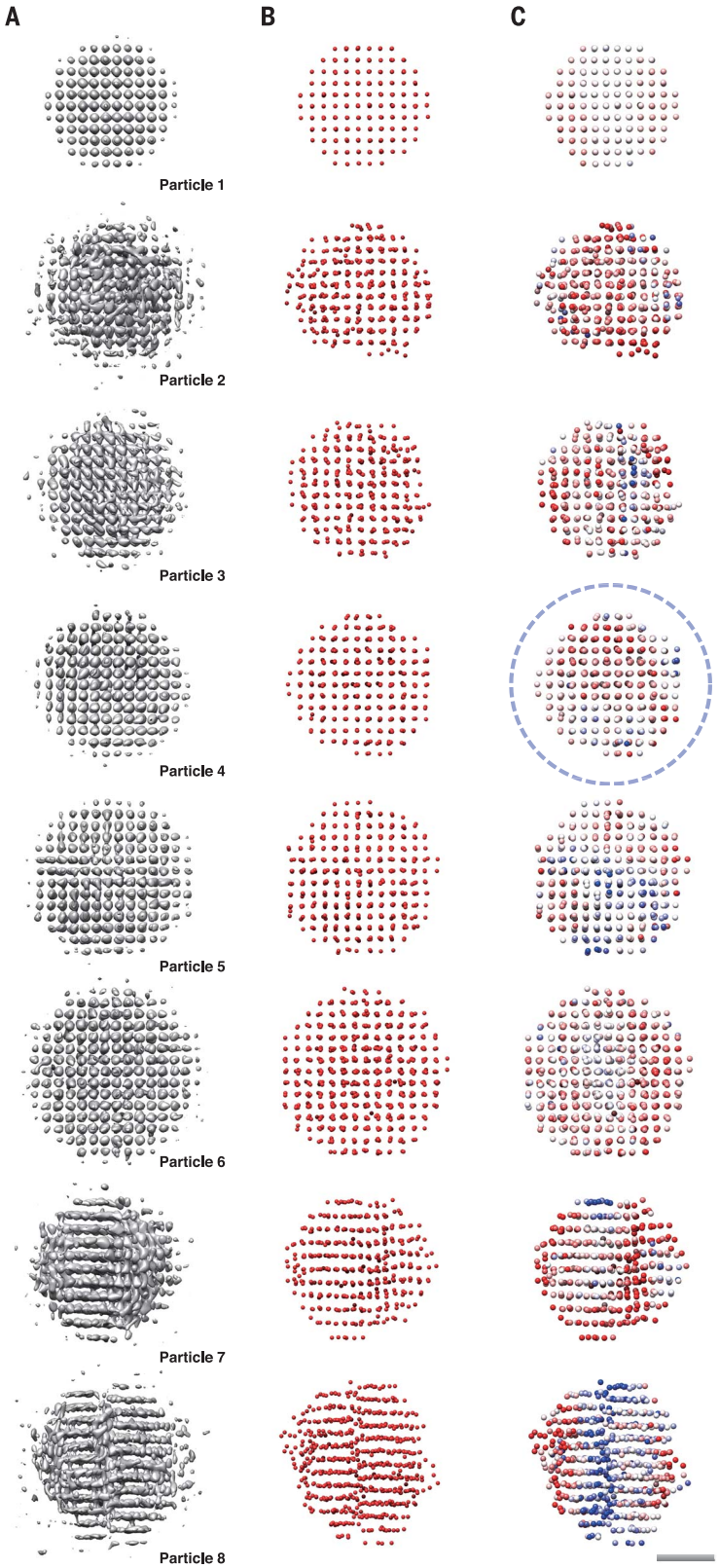

Fig. 1. Atomic-resolution 3D SINGLE for Pt nanocrystals in solution phase. (**A** to **C**) Isosurfaces of high-resolution 3D density maps (A), atomic position maps (B), and strain (ε_{xx}) maps (C) of eight individual nanocrystals (particles 1 to 8). (**D**) Sliced images of the strain (ε_{xx}) map of particle 4. Strain is indicated by the color scale. Scale bar, 1 nm.

method in the presence of the substantial random noise that originates from TEM imaging of liquid, multislice simulated TEM images, including model nanocrystals and water molecules that continuously change orientation and geometry, were generated by using molecular dynamics simulation and used for successful verification of 3D reconstruction (see supplementary materials and figs. S10 and S11). Second, to validate the experimental 3D structures, we confirmed that reprojected images of the obtained 3D electron density maps were in good agreement with the original projections (figs. S12 and S13). Third, we repeated the reconstruction process by using simulated

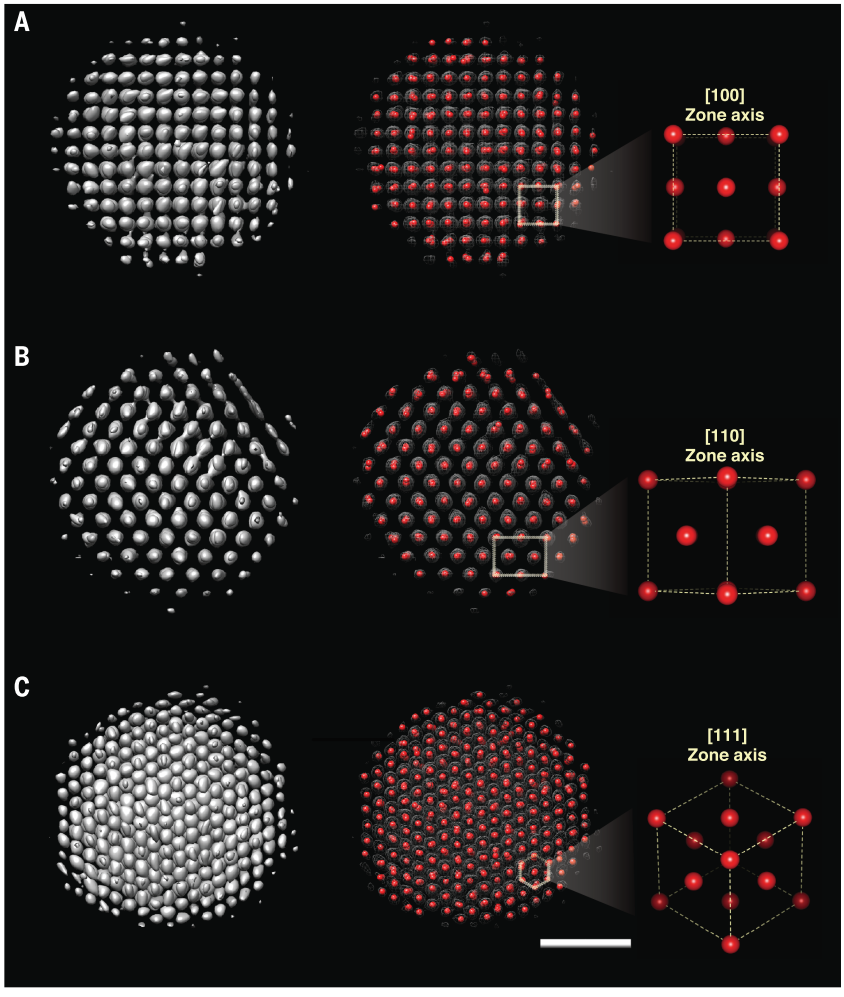

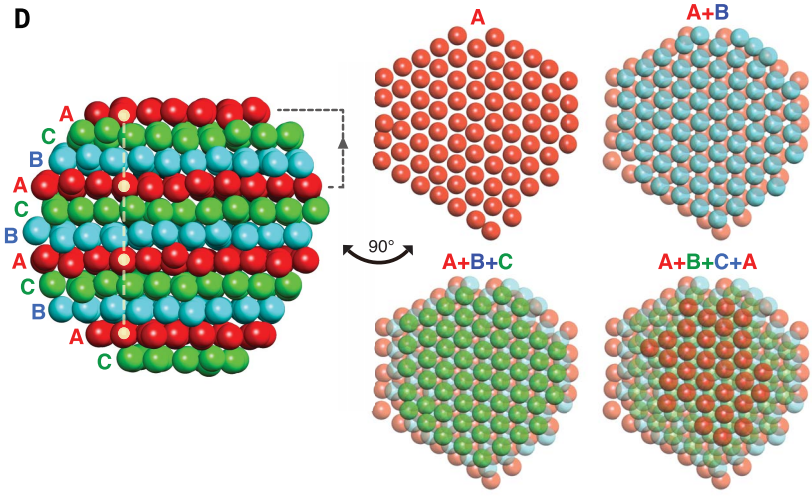

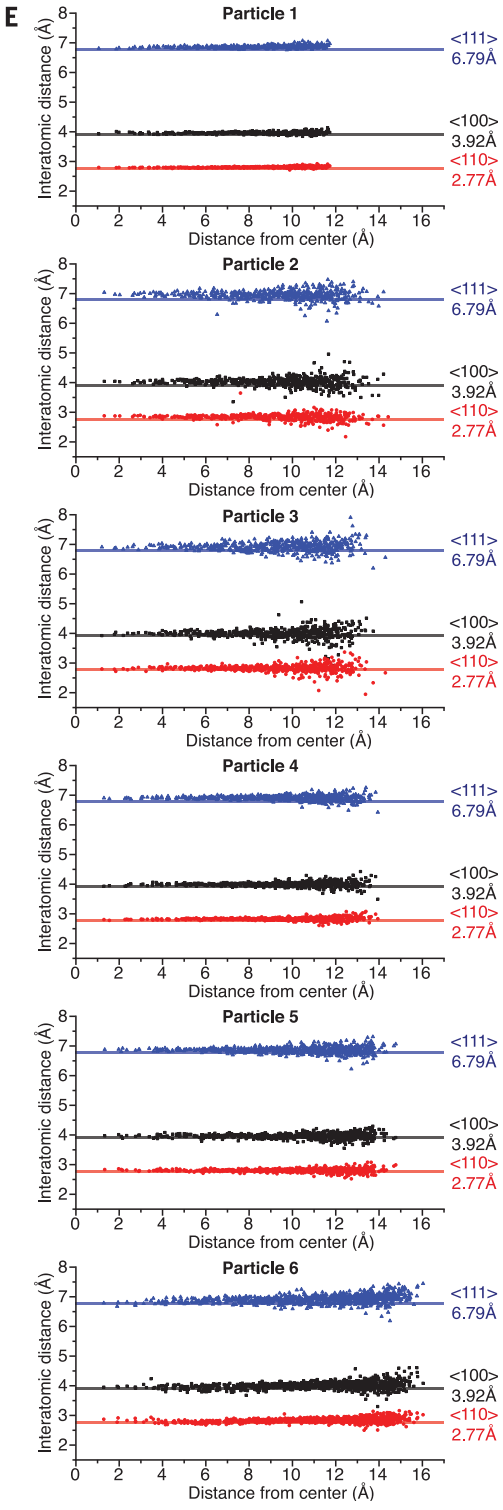

Fig. 2. Atomic-structure analysis of single-crystalline Pt nanocrystals reveals progressive disorder close to the surface. (**A** to **C**) 3D density maps and atomic positions of particle 4 along the [100] (A), [110] (B), and [111] (C) zone axes. Scale bar, 1 nm. (**D**) Packing structure of the nanocrystal. A, B, and C represent repeating lattice planes in fcc crystal structure along the [111] zone axis. (**E**) Interatomic distances in the directions of <110> (red), <100> (black), and <111> (blue) for nanocrystals with six different sizes (particles 1 to 6).

images obtained by multislice simulation of the atomic position map and measured the similarity between the 3D atomic structures from the original TEM images and the simulated images (fig. S14). The average root mean square difference is 9.9 to 19 pm (fig. S14). In addition, the projection directions of the rotating nanocrystals show wide coverage (fig. S15), indicating that the 3D maps include ample crystallographic information obtained from numerous zone axes. Experiments on simulated data show that vertical movement of the nanocrystals has a negligible effect on the final atomic structure (fig. S16).

Effects of surface ligands on the 3D atomic structures of Pt nanocrystals

The Pt nanocrystals were prepared by a typical optimized synthesis to make the final population homogeneous in terms of size and shape distribution, but it is widely known that the individual crystal structures do not have identical atomic arrangements owing to the complexity of their growth trajectories (*27*). Our reconstructed 3D density maps (Fig. 1A and fig. S3A) and corresponding atomic coordinate maps (Fig. 1B and fig. S3B) show this expected structural heterogeneity. Many of the nanocrystals from the same synthesis batch are single crystalline with fcc atomic arrangements, with the exception of heterogeneity due to slight variations in diameter of 2.25, 2.41, 2.42, 2.52, 2.66, and 2.92 nm for particles 1 to 6, respectively, as shown in Fig. 1. Some of the nanocrystals incorporate more diversity in their structures. Shear distortions (particle 7

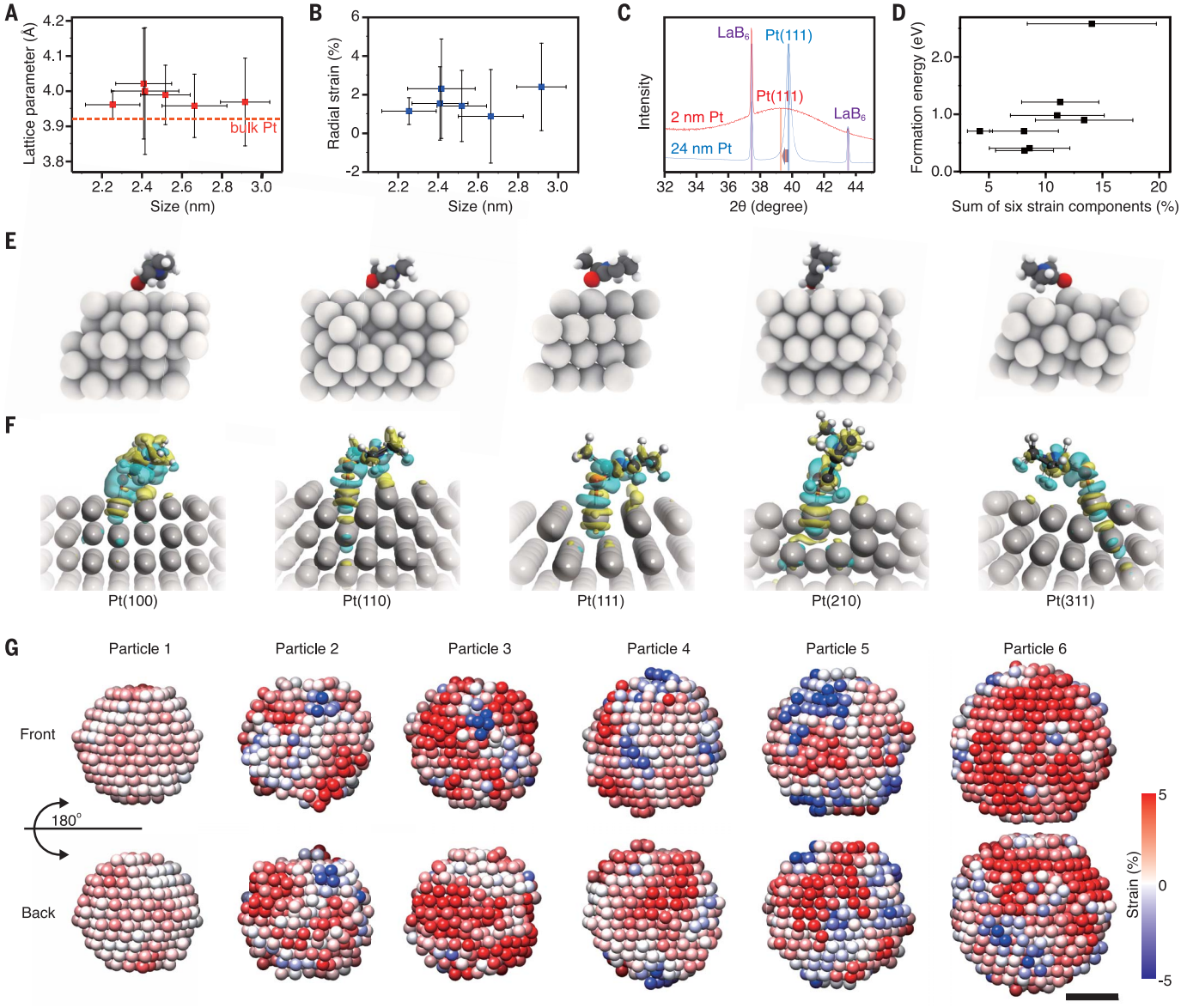

Fig. 3. Size-dependent properties of Pt nanocrystals inferred from their 3D atomic maps. (**A** and **B**) Fitted lattice parameters (A) and averaged radial strain values (B) of single-crystalline nanocrystals with six different sizes. Error bars of *x* axes represent standard deviations of sizes measured in different orientations of individual nanocrystals. Error bars of *y* axes represent standard deviations of averaged interatomic distances along the <100> directions (A) and radial strains (B) of individual atoms. (**C**) XRD patterns of 2-nm-diameter PVP-protected Pt nanocrystals and 24-nm-sized Pt nanocrystals as a reference. (**D**) Formation energy of the reconstructed Pt nanocrystals calculated using their atomic coordinates in a vacuum environment. Error bar represents standard deviation of the sum of six strain components. (**E** and **F**) Binding mode of a PVP ligand onto Pt surfaces with five different planes (E) and its charge density distributions (F). Blue color indicates the electron-deficient region. (**G**) Radial strain maps of the six single-crystalline particles. Strain is indicated by the color scale. Scale bar, 1 nm.

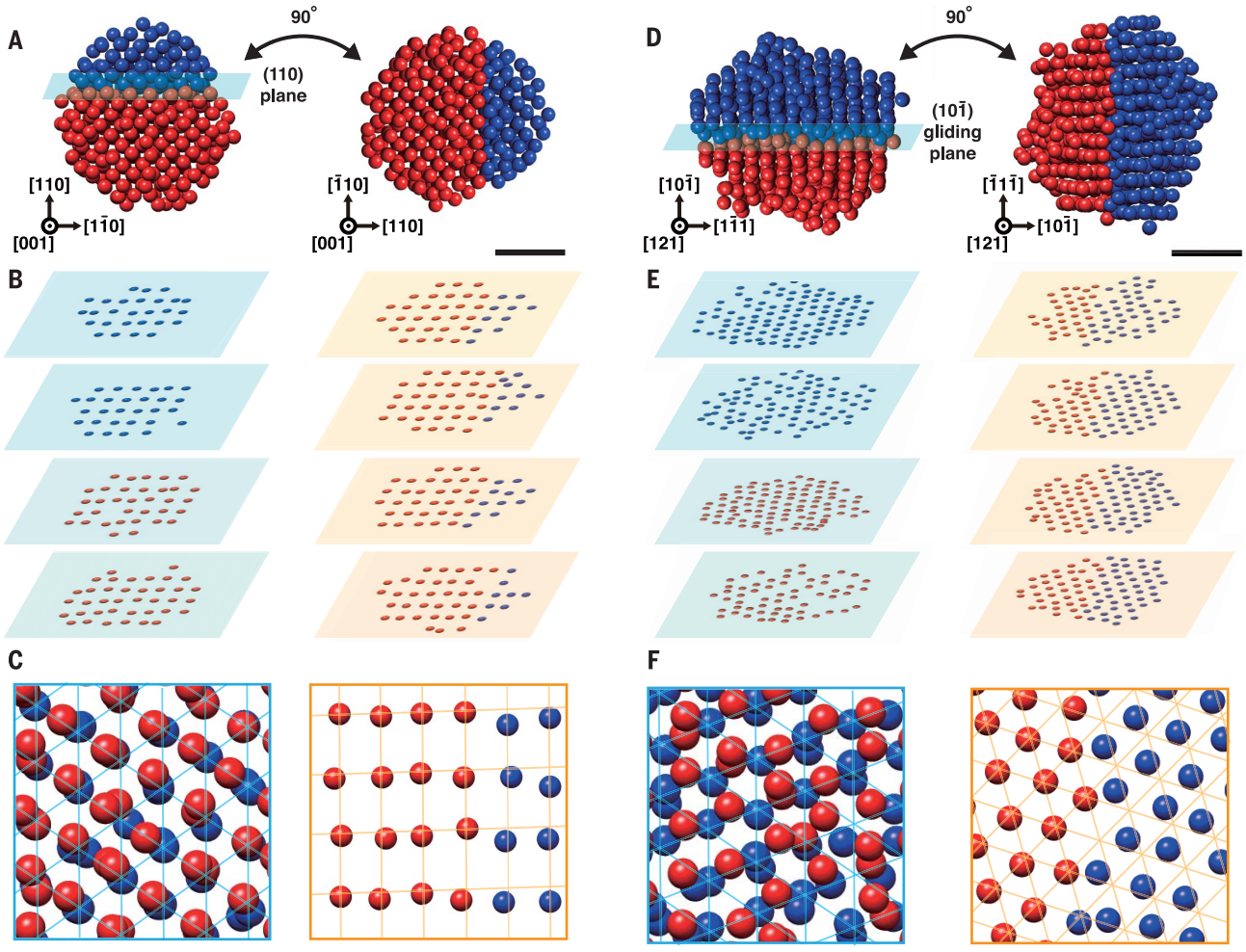

Fig. 4. 3D structure analysis of nanocrystals that have complicated structures. (**A** to **C**) 3D structure analysis of a distorted nanocrystal (particle 7). The overall atomic position map shown along the [001] zone axis appears in (A). Red and blue spheres represent atoms of each domain. Sliced planes of (110) (left) and ($\bar{1}$10) (right) are shown in (B). Superimposed atomic positions of two layers of each domain are shown in (C). (**D** to **F**) 3D structure analysis of a nanocrystal with a dislocation (particle 8). Overall atomic position map shown along the [121] zone axis appears in (D). Sliced planes of (10$\bar{1}$) (left) and ($\bar{1}$1$\bar{1}$) (right) planes are shown in (E). Superimposed atomic positions of two layers of each domain are shown in (F). Scale bars, 1 nm.

in Fig. 1) and dislocations (particle 8 in Fig. 1) are frequently observed in the reconstructed 3D density and atomic position maps.

Our 3D density and atomic position maps match the expected fcc atomic structure. Projections along the [100] zone axis of the 2.52-nm-diameter nanocrystal (particle 4) show that the atoms are positioned with fourfold symmetry at a lattice spacing of 2.0 Å, which corresponds to the Pt (200) plane distance (Fig. 2A). A 45° rotation around [001] (Fig. 2A) reveals a typical lattice projection along the [110] axis with lattice spacing of 2.2-Å {111} and 2.0-Å {200} planes (Fig. 2B). In addition, in a view along the [111] zone axis, the 3D structure exhibits the hexagonal close-packed arrays of atoms (Fig. 2C). The fcc structure can also be identified by an ABC packing sequence along the [111] direction, where every third layer is in the same position (Fig. 2D). Owing to this close-packed structure, the nanocrystals have a coordination number of 12, with the exception of surface atoms (fig. S17).

As nanocrystals become smaller, the fraction of surface atoms becomes substantial. Because they have dangling bonds with surface organic ligands, which is different from the perfect symmetric coordination in a bulk crystal, surface atoms contribute asymmetric atomic orbital overlaps with inner atoms (*28*). In addition, the electronic structure of small nanocrystals can be notably affected by atomic defects (*29*). To understand microscopic structural details of nanocrystals and the extent to which the bulk crystal motif is maintained at the nanoscale level, we measured all interatomic distances along the <111>, <100>, and <110> directions (see the supplementary materials) and plotted them according to the distance from the center (Fig. 2E). Although the interatomic distances are almost constant near the core, they deviate gradually toward the surface, indicating a noticeable deviation of surface atoms from their periodic positions.

By fitting the atomic coordinates, we found an overall expansion of the fcc lattice structure. For example, the lattice parameters of particle 4 are a = 3.990 Å, b = 3.985 Å, c = 3.990 Å, α = 89.96°, β = 89.70°, and γ = 89.75°. Interestingly, such lattice expansion is consistently observed in other nanoparticles (*30*, *31*). The averaged fcc unit-cell lattice constants of the 2.25-, 2.41-, 2.42-, 2.52-, 2.66-, and 2.92-nm-diameter nanocrystals are 3.96, 4.02, 4.00, 3.99, 3.96, and 3.97 Å, respectively, which are 1.02, 2.56, 2.02, 1.74, 0.95, and 1.22% larger than the bulk values, respectively (Fig. 3A). The lattice expansion can be effectively described by the radial strain (ε_{rr}), which is

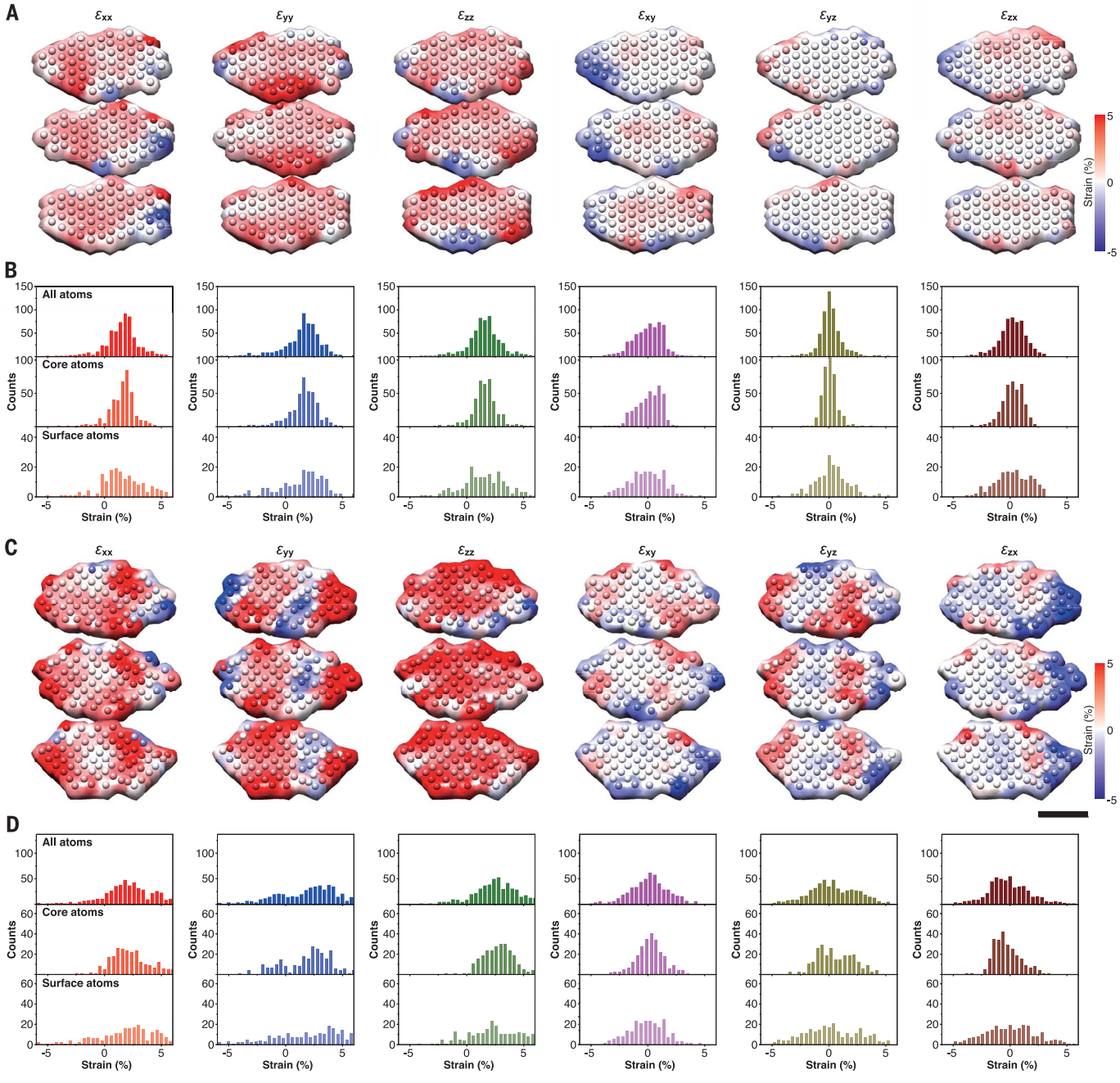

Fig. 5. 3D strain tensor analysis of Pt nanocrystals. (**A**) Sliced maps of the six components of the strain tensors for a single-crystalline particle (particle 4). (**B**) Histograms of the strain tensors of all atoms (top), core atoms (middle), and surface atoms (bottom) of particle 4. (**C**) Sliced maps of the six components of the strain tensors for a particle with a distorted lattice (particle 7). Scale bar, 1 nm. (**D**) Histograms of the strain tensors of all atoms (top), core atoms (middle), and surface atoms (bottom) of particle 7. In (A) and (C), strain is indicated by the color scale.

defined as $\varepsilon_{rr} = \frac{\partial u_r}{\partial r}$, where r is the distance between an atom and the center of mass of a particle and u_r is radial displacement (fig. S18). Consistent with our observed deviations of lattice parameters, the arithmetic mean (averaged over all atom positions) radial strain is positive for particles 1 through 6 (Fig. 3B). We revisited previous x-ray diffraction (XRD) studies of ligand-protected nanocrystals and found that such lattice expansion, which was unrecognized because the peak shift was very small, is observed consistently in polyvinylpyrrolidone (PVP)–protected metal nanocrystals (*30*, *31*). We also checked our PVP-protected Pt nanocrystals using synchrotron XRD experiments. XRD patterns exhibit a slightly enlarged lattice parameter (3.976 Å) compared with that of bulk Pt (Fig. 3C). These observations imply that crystal structures of Pt nanocrystals tend to expand slightly when protected by PVP surface ligands in the native solution phase. These results are in contrast to lattice compressions theoretically observed for metal nanocrystals without protecting ligands,

which is explained by the effect of surface tension and strong bonding of surface atoms with low coordination numbers (*6*). Our results indicate that such effects can be weakened and even reversed when surface ligands are adsorbed on the metal nanocrystals in the solution phase. We performed density functional theory (DFT) calculations and show that the adsorption of PVP ligands can induce localization of electron density around surface Pt atoms. As a result, the inward metallic bonds are weakened as the atomic distance increases (Fig. 3, E and F). Because the PVP ligands are long polymers decorated with multiple binding functional groups, the coverage of polymeric binding may not be uniform across the surface. This is likely to induce local deviation of the atomic lattice and the resulting surface strain. Particular surface regions of a Pt nanocrystal, where binding of pyrrolidone groups are more dominant, are presumably expanded. Our radial strain measurements show such a localization on specific surface regions of the particle (see Fig. 3G).

The observed lattice fluctuations and the expansion of the fcc crystal structure are difficult to measure in conventional high-resolution TEM images of nanocrystals because the interatomic distances are averaged over each atomic column along the projection direction. Further, motion in the liquid makes it difficult to capture the correct zone axis with the high precision that is required. Our atomic-resolution 3D SINGLE method overcomes these limitations and allows measurement of the interatomic distances between all constituent atoms in 3D space, enabling detailed structural characterization. We confirmed that the lattice fluctuations are not due to inaccuracy of the reconstruction method. Accurate interatomic distances were measured in the 3D atomic position map generated from reconstructing simulated noisy TEM images of a model nanocrystal with a perfect fcc structure. The interatomic distances consistently follow bulk fcc parameters with a very marginal deviation throughout the volume of the nanocrystal (fig. S7C). Thus, the observed deviation of the lattice parameter is inherent to these small ligand-protected Pt nanocrystals.

By using the experimentally determined atomic positions, the formation energy of each nanocrystal can be directly evaluated using DFT calculation without relaxation processes. Overall, the higher-strained particles require a higher formation energy, as shown in Fig. 3D (see supplementary materials). Highly strained nanocrystals, such as distorted particles, show high formation energies attributed to the strain field (Fig. 3D). It is possible that the energetically metastable structures, including the dislocations, are kinetically trapped during complicated synthetic reactions that incorporate particle coalescence (*23*). The DFT calculation considered bare surfaces for reliable comparison between nanocrystals without uncertainty originating from the complexity of ligand passivation (table S1). By considering the stabilization effect of surface binding groups, the formation energy of nanocrystals with PVP ligands can be substantially reduced (fig. S19 and table S2).

Structural heterogeneity of Pt nanocrystals

Our 3D density and atomic position maps reveal that Pt nanocrystals have more complicated crystal structures than the single-crystalline fcc structure. The atomic arrangement of the distorted nanocrystal (particle 7) is slightly bent around a (110) plane (Fig. 4, A to C). Overlaying different atomic planes from each domain as red and blue reveals that the lattice points of the two domains are slightly mismatched (Fig. 4C). In addition, several vacancies are observed near the boundary (Fig. 4B).

Particle 8 has a $(1\bar{1}1)$ partial edge dislocation, as viewed along a [121] zone axis in Fig. 4D. This is a Shockley partial dislocation with the Burger's vector of $a/2\langle 111\rangle$ and a gliding plane of $(10\bar{1})$. The atoms near the dislocation are highly disordered (Fig. 4E), whereas other atoms conform to an fcc lattice. A magnified image of a $(1\bar{1}1)$ plane (Fig. 4F), which is perpendicular to the gliding plane, shows a hexagonal array within each domain and breakage of periodicity near the boundary between the two domains. The origin of the disordered structure of the nanocrystal can be explained by coalescence events during the formation of the nanocrystals (*23*, *32*). Recent liquid-phase TEM studies have revealed that Pt nanocrystals frequently coalesce along low-index surfaces and become multidomain structures when they grow by an aggregative pathway (*23*, *27*, *33*, *34*).

Strain analysis of individual Pt nanocrystals from the 3D atomic maps

Strain imposed on the constituent atoms determines catalytic activities of metal nanocrystals because the strain modifies the local binding energy with adsorbates by changing the bandwidth of d orbitals (*35*). Engineering tensile strain is indeed successfully applied in tuning reactivity of Pt nanocrystals in many important catalytic reactions, including the methanol oxidation reaction and the oxygen reduction reaction (*36*, *37*). Strain analysis at high resolution will be an important asset in understanding catalytic performance of heterogeneous catalysts and tuning their performance. Using the fcc structure with a best-fit lattice parameter as a reference, we obtained 3D strain maps by calculating the atomic displacement field, convolving it with a 2-Å-wide 3D Gaussian kernel, and differentiating it (Fig. 5 and figs. S20 and S21) (*17*). We also used geometric phase analysis (*38*) for comparison. Both methods showed similar results (fig. S22). The full six-element strain tensor of particle 4 is mapped for each atomic position in 3D space (Fig. 5A). The strain maps clearly show that the surface of the nanocrystals has larger strain compared with the core atoms (Figs. 1D and 5B). The strain distributions of the surface atoms—defined as $r > R - d_{111}$, where r is the distance of an atom from the center of mass, R is the radius of the nanocrystal, and d_{111} is the bulk Pt(111) plane distance—are 1.89, 2.27, 1.92, 1.54, 1.49, and 1.52%, whereas those of core atoms are 1.14, 1.28, 1.15, 1.07, 0.66, and 0.93% for ε_{xx}, ε_{yy}, ε_{zz}, ε_{xy}, ε_{yz}, and ε_{zx}, respectively (Fig. 5B and fig. S23). The broader strain distribution of the surface atoms is due to the disorder of the surface atoms, presumed to be accommodated by surface ligand protection. Tensile strain occurs throughout the nanocrystal for both surface and core atoms. The average strains of ε_{xx}, ε_{yy}, and ε_{zz} (parallel to the <100> directions) for particle 4 are 1.54, 1.49, and 1.58%, respectively, consistent with the expanded lattice parameters obtained by fitting of the atomic coordinates.

The distorted Pt nanocrystal (particle 7) also shows tensile strain throughout the nanocrystal and large strain distribution on the surface. Owing to its structural deformation, the strain distribution of the distorted particle is 2.23%, which is 1.7 times broader than that of the single crystal (particle 4; 1.31%). In addition, the bent structure leads to high shear strain of atoms at the domain boundary (Fig. 5C), resulting in a bimodal shear strain distribution with two distribution centers (Fig. 5D). The nanocrystal with the dislocation also shows large strains at the domain boundary (particle 8 in Fig. 1C), which is known to enhance catalytic activities (*39*).

Conclusion

We show that high-resolution 3D atomic arrangements of Pt nanocrystals synthesized from a single batch have critical structural differences. This was made possible by the development of atomic-resolution 3D SINGLE for solving the structure of nanocrystals in solution phase. Our results can be understood by the nature of typical colloidal synthesis of nanocrystals, which thermodynamically deviates from expectations based on bulk crystallography. Structure and strain analysis enabled by assignment of precise atomic positions reveals lattice expansions of ligand-protected metal nanocrystals in solution and the existence of large strain near domain boundaries, dislocation edges, and surfaces. The detailed structural information we introduce is strongly linked to the origin of the catalytic performance of Pt nanocrystals. We also demonstrate that the precise atomic structures obtained by our approach can be utilized in computational chemistry to improve the accuracy of property

predictions of nanocrystals. Atomic-resolution 3D SINGLE can be applied to nanocrystals with various composition (fig. S24) and atomic structural integrity. It will find applications in other systems, including colloidal nanomaterials and biological macromolecules, where structural information in solution is required.

REFERENCES AND NOTES

1. M. A. Pfeifer, G. J. Williams, I. A. Vartanyants, R. Harder, I. K. Robinson, *Nature* **442**, 63–66 (2006).
2. M. Cargnello *et al*., *Science* **341**, 771–773 (2013).
3. L. Hultman *et al*., *Phys. Rev. Lett.* **87**, 225503 (2001).
4. M. Azubel *et al*., *Science* **345**, 909–912 (2014).
5. T. Nilsson Pingel, M. Jørgensen, A. B. Yankovich, H. Grönbeck, E. Olsson, *Nat. Commun.* **9**, 2722 (2018).
6. Z. Huang, P. Thomson, S. Di, *J. Phys. Chem. Solids* **68**, 530–535 (2007).
7. L. Chen, P. Fleming, V. Morris, J. D. Holmes, M. A. Morris, *J. Phys. Chem. C* **114**, 12909–12919 (2010).
8. Y. Negishi *et al*., *J. Am. Chem. Soc.* **137**, 1206–1212 (2015).
9. W. Zhu *et al*., *J. Am. Chem. Soc.* **136**, 16132–16135 (2014).
10. S. G. Kwon, T. Hyeon, *Small* **7**, 2685–2702 (2011).
11. W. Gao *et al*., *Sci. Adv.* **5**, eaau9590 (2019).
12. Z. Fan *et al*., *Nat. Commun.* **6**, 6571 (2015).
13. W. Wu, E. V. Shevchenko, *J. Nanopart. Res.* **20**, 255 (2018).
14. K. Yang *et al*., *J. Mater. Chem. A Mater. Energy Sustain.* **7**, 3863–3873 (2019).
15. F. Bertolotti *et al*., *Nat. Mater.* **15**, 987–994 (2016).
16. T. Altantzis *et al*., *Nano Lett.* **19**, 477–481 (2019).
17. R. Xu *et al*., *Nat. Mater.* **14**, 1099–1103 (2015).
18. Y. Yang *et al*., *Nature* **542**, 75–79 (2017).
19. B. Goris *et al*., *Nat. Mater.* **11**, 930–935 (2012).
20. J. Miao, P. Ercius, S. J. L. Billinge, *Science* **353**, aaf2157 (2016).
21. A. Bartesaghi *et al*., *J. Struct. Biol.* **162**, 436–450 (2008).
22. Y. Cheng, *Cell* **161**, 450–457 (2015).
23. J. Park *et al*., *Science* **349**, 290–295 (2015).
24. C. F. Reboul, M. Eager, D. Elmlund, H. Elmlund, *Protein Sci.* **27**, 51–61 (2018).
25. M. van Heel, M. Schatz, *J. Struct. Biol.* **151**, 250–262 (2005).
26. E. J. Kirkland, *Advanced Computing in Electron Microscopy* (Springer, 2010).
27. J. M. Yuk *et al*., *Science* **336**, 61–64 (2012).
28. S. Baumann *et al*., *Science* **350**, 417–420 (2015).
29. A. D. P. Leach *et al*., *J. Phys. Chem. C* **120**, 5207–5212 (2016).
30. T. Teranishi, M. Hosoe, T. Tanaka, M. Miyake, *J. Phys. Chem. B* **103**, 3818–3827 (1999).
31. C. Song *et al*., *Sci. Rep.* **6**, 31400 (2016).
32. J. C. Ondry, M. R. Hauwiller, A. P. Alivisatos, *ACS Nano* **12**, 3178–3189 (2018).
33. D. Li *et al*., *Science* **336**, 1014–1018 (2012).
34. B. Luo *et al*., *ACS Nano* **11**, 7626–7633 (2017).
35. M. Mavrikakis, B. Hammer, J. K. Nørskov, *Phys. Rev. Lett.* **81**, 2819–2822 (1998).
36. P. Strasser *et al*., *Nat. Chem.* **2**, 454–460 (2010).
37. X. Huang *et al*., *Science* **348**, 1230–1234 (2015).
38. M. J. Hÿtch, E. Snoeck, R. Kilaas, *Ultramicroscopy* **74**, 131–146 (1998).
39. R. G. Mariano, K. McKelvey, H. S. White, M. W. Kanan, *Science* **358**, 1187–1192 (2017).

ACKNOWLEDGMENTS

The experiments performed at the Molecular Foundry, Lawrence Berkeley National Laboratory, were supported by the U.S. Department of Energy (DOE) under contract no. DE-AC02-05CH11231. **Funding:** J.P. and T.H. acknowledge the Institutes for Basic Science (IBS-R006-D1). J.P. acknowledges National Research Foundation of Korea (NRF) grants funded by the Korean government (MSIT) (nos. NRF-2017R1C1B2010434, NRF-2017R1A5A1015365, and NRF-2019M3E6A1064877); the Ministry of Trade, Industry, and Energy (MOTIE); and the Korea Semiconductor Research Consortium (KRSC) support program for the development of future semiconductor devices (no. 10080657). B.H.K., J.H., S.K., and J.P. acknowledge support from the Samsung Science and Technology Foundation under project number SSTF-BA1802-08 for the development of the reconstruction algorithm. H.E. acknowledges Australian Research Council (ARC) grant DP170101850 and National Health and Medical Research Council, Australia, grant APP1125909. C.F.R. acknowledges an Early Career Fellowship (APP1122769). P.E. acknowledges the DOE, Office of Basic Energy Sciences, Materials Sciences and Engineering Division, under contract no. KC22ZH. A.P.A. acknowledges support from the DOE, Office of Science, Office of Basic Energy Sciences, Materials Sciences and Engineering Division, under contract no. DE-AC02-05-CH11231 within the Physical Chemistry of Inorganic Nanostructures Program (KC3103). H.C. and B.H. were supported by the Creative Materials Discovery Program through the NRF funded by the Ministry of Science and ICT (NRF-2017M3D1A1039287) and the Global Frontier Program through the Global Frontier Hybrid Interface Materials (GFHIM) of the NRF funded by the Ministry of Science and ICT (project no. 2013M3A6B1078882). **Author contributions:** B.H.K. and J.H. contributed equally to this work. B.H.K., J.H., P.E., H.E., and J.P. planned the research. B.H.K., P.E., and J.P. discussed and/or acquired the data. B.H.K., J.H., S.K., C.F.R., and H.E. conducted the image reconstruction. B.H.K., J.H., S.K., A.P.A., T.H., P.E., H.E., and J.P. analyzed and interpreted the results. H.C., D.K., H.B., H.L., and B.H. performed the DFT calculations and molecular dynamics simulations. B.H.K., H.H., and J.L. obtained the XRD pattern. B.H.K., J.H., P.E., H.E., and J.P. wrote the manuscript. P.E., H.E., and J.P. supervised the research. All authors contributed to the discussion of results. **Competing interests:** The authors declare no competing financial interests. **Data and materials availability:** All data are available in the main text or the supplementary materials.

SUPPLEMENTARY MATERIALS

science.sciencemag.org/content/368/6486/60/suppl/DC1
Materials and Methods
Figs. S1 to S24
Tables S1 and S2
References (*40*–*42*)
Movies S1 and S2

13 March 2019; accepted 20 February 2020
10.1126/science.aax3233

Science

Critical differences in 3D atomic structure of individual ligand-protected nanocrystals in solution

Byung Hyo KimJunyoung HeoSungin KimCyril F. ReboulHoje ChunDohun KangHyeonhu BaeHyejeong HyunJongwoo LimHoonkyung LeeByungchan HanTaeghwan HyeonA. Paul AlivisatosPeter ErciusHans ElmlundJungwon Park

Science, 368 (6486), • DOI: 10.1126/science.aax3233

Seeing subtle nanoparticle differences

A challenge in the fabrication of nanoparticles is that even for particles of uniform size, there will still be a distribution in the atomic arrangements and surface capping ligands from one particle to the next. Using liquid-cell transmission electron microscopy, Kim *et al.* reconstructed the structure of individual nanocrystals synthesized in one batch while they were still in solution. A comparison of multiple particles showed structural heterogeneity and differences between the interior and the outer shell of the individual nanoparticles, as well as nanoparticles containing extended defects and thus differences in internal strain, all of which can affect the physical and chemical properties of each particle.

Science, this issue p. 60

Science (ISSN 1095-9203) is published by the American Association for the Advancement of Science. 1200 New York Avenue NW, Washington, DC 20005. The title *Science* is a registered trademark of AAAS.